JOURNAL OF MATERIALS SCIENCE 31 (1996) 4883–4889

Coherency strain effects on TEM images of composite precipitates in Al–Li–Zr alloys

M. K. AYDINOL, A. S. BOR
Metallurgical Engineering Department, Middle East Technical University, Ankara, 06531, Turkey

Anomalous superlattice dark-field images of composite precipitates consisting of a dark core surrounded by a bright shell in Al–2.52Li–0.15Zr alloys, has been investigated by many beam dynamical image simulations employing a scattering matrix approach. The coherency strain field in the shell of the precipitate, as well as in the matrix, has been calculated by use of relations derived, and these are incorporated into the image calculations to determine whether the unexpected images can be elucidated by the coherency strain field of the precipitates. It has been found that the coherency strain field may modify the observed composite precipitate images, but it definitely cannot be the origin of the observed anomaly in these images. It has been also shown by the image matching technique, that the mismatch between the β′ (Al_3Zr) precipitates and aluminium matrix in Al–Li–Zr alloys should have a value of about 0.3%.

1. Introduction

The transmission electron microscope (TEM) images of composite precipitates formed by epitaxial nucleation of δ′ (Al_3Li) phase on the already existing β′ (Al_3Zr) particles [1,2] to form a uniform shell around them is an interesting feature of zirconium-containing Al–Li alloys. Both Al_3Zr and Al_3Li phases have ordered $L1_2$ crystal structure and their lattice parameters are very close to each other. Because, in addition, both phases have cube–cube orientation relationship with the aluminium matrix, their individual electron diffraction patterns coincide. Therefore, dark-field images of composite precipitates taken from any superlattice reflection, which is common to both phases, are ordinarily expected to be completely bright. However, the superlattice dark-field TEM images of these precipitates are composed of a dark core surrounded by a bright shell. In previous studies, lack of contrast from the β′ particles constituting the core of the composite precipitates has been attributed to (i) decay in the structure factor upon substitution of zirconium atoms by lithium in the β′ phase [3,4], (ii) coherency strains causing variable projected potentials for different columns across the composite precipitate [5], (iii) inelastic scattering phenomena [6], (iv) cored structure of the composite precipitates [7], and (v) slight tilt of the β′ phase from the exact cube–cube orientation relationship [8]. Among the above predictions, only the first two seem to be worth considering, because the others can be readily nullified by diffraction and imaging studies. The proposal of Gayle and Vandersande [3,4] that lithium atoms may be substituted in the β′ phase has been supported by kinematical image calculations, but still number of questions can be raised on the validity of their prediction if the kinetics of precipitation is taken into account. The strain effect mentioned by Makin *et al.* [5] may be of importance, but has not yet been subject to any quantitative analysis.

In the present study, the origin of the dark core image of composite precipitates has been investigated by dynamical image simulation technique, to determine whether this unexpected image can be elucidated by the coherency strain field of these precipitates.

2. Image simulation technique

The superlattice dark-field images of composite precipitates in Al–Li–Zr alloys have been computed by using the scattering matrix method of many beam dynamical theories of electron diffraction [9]. In the case of two beams, $n = 2$, if $\phi_0(0)$ and $\phi_g(0)$ are the amplitudes of the transmitted and diffracted beams entering a perfect crystal of thickness, z, then the amplitudes of the outgoing waves, $\phi_0(z)$ and $\phi_g(z)$, can be represented as

$$\begin{bmatrix}\phi_0(z)\\ \phi_g(z)\end{bmatrix} = \boldsymbol{S}\begin{bmatrix}\phi_0(0)\\ \phi_g(0)\end{bmatrix} \quad (1)$$

where $\boldsymbol{S}$ is the scattering matrix equal to

$$\boldsymbol{S} = \boldsymbol{C}\{e^{2\pi i\gamma^{(n)}z}\}\boldsymbol{C}^{-1} \quad (2)$$

where $\{\}$ represents the diagonal matrix whose elements are all zero except for the diagonal. The elements of the matrix $\boldsymbol{C}$ originates from the amplitudes of the Bloch waves and can be found by solving the eigen equation [10]

$$\boldsymbol{A}\boldsymbol{C} - \gamma\boldsymbol{C} = 0 \quad (3)$$

0022–2461

where A is an $n \times n$ complex matrix, and contains the information on the periodic potential in its off-diagonal and crystal orientation in its diagonal elements [10, 11]

$$A_{00} = \frac{i}{2\xi'_0} \tag{4a}$$

$$A_{gg} = s + \frac{i}{2\xi'_0} \tag{4b}$$

$$A_{gg'} = \frac{1}{2\xi_{g-g'}} + \frac{i}{2\xi'_{g-g'}} \tag{4c}$$

where i is the complex number, ξ_g is the extinction distance, ξ'_g and ξ'_0 are the anomalous and normal absorption distances and s is the deviation parameter. Once the elements of matrix A have been determined, Equation 3 has to be solved to find the eigen vectors C, and the eigen values γ to construct the scattering matrix belonging to the given perfect crystal of thickness z. The amplitudes of the beams leaving the crystal can be calculated from Equation 1 and the intensities of the beams by squaring the amplitude, $I \propto \phi\phi^*$.

When there is a planar defect, such as a stacking fault, dividing the perfect crystal into two slabs with a relative displacement R between them, the problem can be solved by introducing a matrix F, which represents the phase shift in the beams by an amount α due to the displacement R. In case of two beams,

$$F = \begin{bmatrix} 1 & 0 \\ 0 & e^{-i\alpha} \end{bmatrix} \tag{5}$$

where $\alpha = 2\pi g \cdot R$. Then, the diffracted amplitude will be

$$\phi(z) = S_2 F S_1 \phi(0) \tag{6}$$

where S_1 and S_2 are the scattering matrices of the perfect crystals above and below the fault, respectively.

In imperfect crystals with continuously varying strain field, the position-dependent defect displacement vector R causes the reflecting planes to be curved with the consequence that the deviation parameter, s, varies continuously throughout the crystal. Ordinarily, intensity calculation in such crystals requires the column under consideration to be divided into thin slices, each with a different s value and therefore with a different scattering matrix. Alternative to this lengthy calculation procedure, imperfect crystals with continuously varying strain fields can be approximated as an assemblage of effectively thin slabs of perfect crystal of thickness dz with relative displacements rather than rotations between them. Then the amplitudes of the beams will be

$$\phi(z) = S_m F_{m-1} S_{m-1} F_{m-2} \cdots S_2 F_1 S \phi(0) \tag{7}$$

where m is the number of the slabs, S_k, $k = 1 - m$, are the scattering matrices of the slabs and F_k are the fault matrices constructed according to Equation 5 using the strain-originated relative displacements between the consecutive slabs. Because slab thickness and orientation are constant, S_k are the same for all slabs, resulting in considerable economy in the calculation scheme.

The images of composite precipitates were simulated by use of a computer program developed in Pascal programming language for many beam-image simulations employing the above principles of the scattering matrix approach [12]. In the simulations, five systematical beams, namely $(\bar{1}\,0\,0)_{S_2}$, $(0\,0\,0)_{Tr}$, $(1\,0\,0)_{S_1}$, $(2\,0\,0)_F$ and $(3\,0\,0)_{S_3}$ were considered. If only two beams have been used, the (1 0 0) superlattice and (0 0 0) transmitted beams, then the superlattice beam leaving the precipitate would not interact with the transmitted beam until it reaches the exit side of the foil as if it is travelling in a vacuum, and the thickness of the aluminium layer beneath the precipitate would have no effect on the image. However, this does not seem to be realistic, because it is obvious that under identical conditions, i.e. both in size and position through the thickness of the foil, precipitates give rise to brighter images in thin sections compared to those in thick sections, Fig. 1.

In the five-beam calculations, Fig. 2, in the matrix layer above the precipitate, only two beams, the fundamental (F) and the transmitted (Tr), were employed

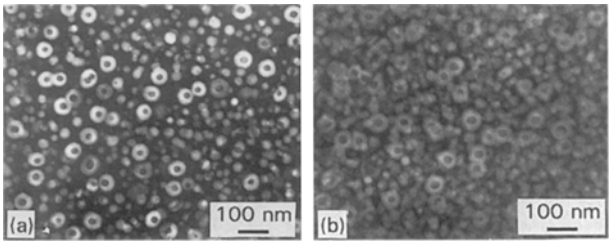

Figure 1 TEM images of precipitates, $g = (1\,0\,0)$, $s = 0$, in the same specimen in (a) thin and (b) thick sections.

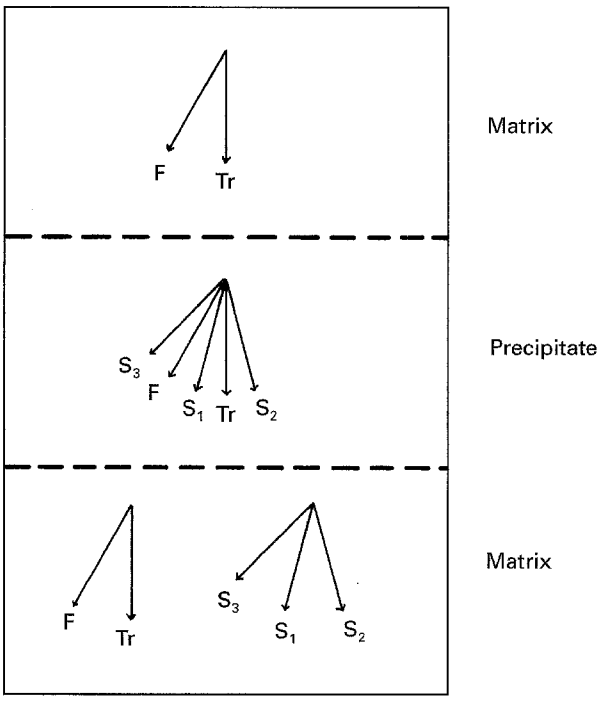

Figure 2 Schematic representation of the beams used in the image calculation scheme.

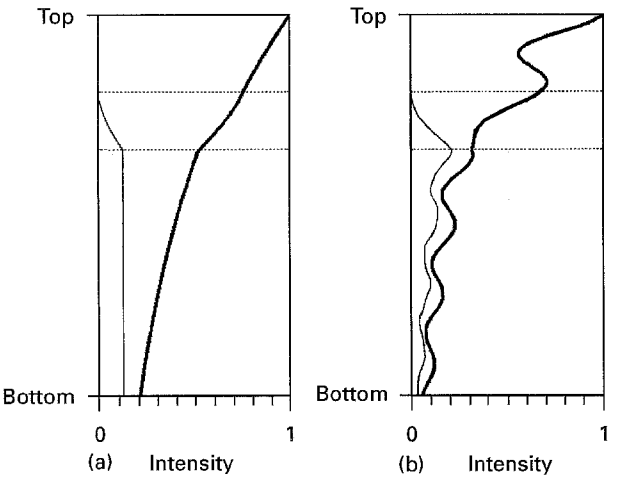

Figure 3 (——) The intensity profiles of the superlattice beam, $g = (1\,0\,0)$, $s = 0$ and (—) the transmitted beam in the cored region of the composite precipitate through the thickness of the foil using (a) two and (b) five systematic beams.

in calculations because the superlattice reflections are forbidden in the aluminium matrix. Reaching the composite precipitate, calculations have been extended to five beams, namely the fundamental (F), the three systematic superlattice (S_1, S_2 and S_3) and the transmitted (Tr) beams. After leaving the precipitate phase, the three superlattice beams travelling through the matrix beneath the precipitate and related to each other by the Bragg angle, are expected to interact with each other, while the transmitted and the fundamental beams leaving the precipitate phase go on to travel as a pair without interacting with the superlattice beams. Therefore, the calculations were carried out as if two independent diffraction phenomena are taking place concurrently: one with two beams, Tr and F, and the other with three superlattice beams S_1, S_2 and S_3. Beams in each set are related to each other by the Bragg angle and interact with each other only within that set. The intensity of the (1 0 0) superlattice beam of the second set at the exit side of the foil was used in image construction. Such interaction of superlattice beams during their travel in the matrix after leaving the precipitate has not been taken into consideration in previous image simulation studies. The importance of including the interaction between the superlattice beams in the matrix beneath the precipitate is evident in Fig. 3, which shows the variation of superlattice beam intensity as a function of depth through the thickness of the foil with a precipitate. While the superlattice beam, assumed not to interact with any other beam after leaving the precipitate phase, reaches the bottom of the foil with constant intensity unaffected by foil thickness, Fig. 3a, the superlattice beam interacting with other superlattice beams decays in an oscillating manner, giving rise to lower intensities as the thickness of the foil increases, Fig. 3b.

3. Evaluation of the strain field around spherical composite precipitates

Coherent single precipitates of Al_3Zr phase are expected to produce coherency strains in the matrix while the precipitates themselves are strained uniformly. In case of composite precipitates, the strain field must distribute over the shell as well as in the matrix and this would contribute to the image. To include the effect of the strain in simulating the images of composite precipitates, expressions defining the displacements due to coherency strains both in the shell and the matrix are required. This has been achieved by a derivation starting from the mechanistic approach and then inserting the crystal parameters. The displacements in core, u_C, shell, u_S, and matrix, u_M, at radius r in spherical geometry can be given as [13]

$$u_C = \frac{r}{E_C} P_1 (\nu_C - 1) \tag{8a}$$

$$u_S = \frac{r}{E_S}\left\{\frac{P_2 b^3(2r^3 + a^3)}{2r^3(a^3 - b^3)} - \frac{P_1 a^3(2r^3 + b^3)}{2r^3(a^3 - b^3)} - \nu_S\left(\frac{P_2 b^3(r^3 - a^3)}{r^3(a^3 - b^3)} + \frac{P_1 a^3(b^3 - r^3)}{r^3(a^3 - b^3)}\right)\right\} \tag{8b}$$

$$u_M = \frac{r}{E_M}\left(\frac{1}{2} P_2 \frac{b^3}{r^3} + \nu_M P_2 \frac{b^3}{r^3}\right) \tag{8c}$$

where P_1 and P_2 are the pressures exerted on the boundaries between core and shell, and shell and matrix, respectively, a and b are the constrained radius of the core and shell and E and ν are the elastic modulus and the Poisson's ratio of the corresponding phases, respectively. The displacement equations given above in terms of the elastic properties of the phases and the unknown pressures are a direct consequence of the continuum elasticity theory [13]. The parameters of the phases, i.e. the lattice parameters, and the disregistry between the phases, are introduced into the above formulation considering the transformation geometry, Fig. 4.

Assume that, initially, a sphere of radius r_1 and a hollow sphere of inner radius r_1 and outer radius r_2 are cut and taken out from the matrix, Fig. 4. Then allow these elements to transform to their corresponding phases freely, i.e. inner sphere into Al_3Zr and the hollow sphere into Al_3Li. After the transformation has completed, the radius of the inner sphere will be r_b and the inner and outer radius of the hollow sphere will be r_{d1} and r_{d2} respectively, due to the volume changes during transformation. Let $\Delta V_{\alpha-\beta'}$ and $\Delta V_{\alpha-\delta'}$ be the fractional volume changes during transformation

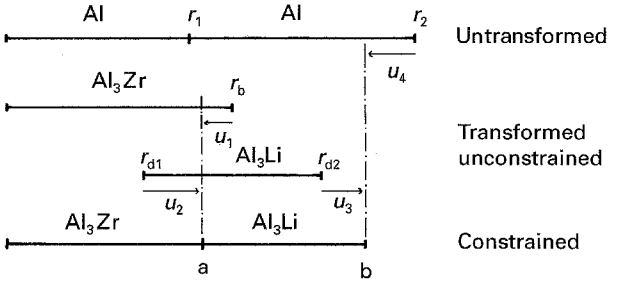

Figure 4 Definition of displacement vectors due to mismatch.

from aluminium to Al_3Zr and aluminium to Al_3Li, respectively, so that

$$r_b^3 = r_1^3(1 + \Delta V_{\alpha-\beta'}) \quad (9a)$$

$$r_{d1}^3 = r_1^3(1 + \Delta V_{\alpha-\delta'}) \quad (9b)$$

$$r_{d2}^3 = r_2^3(1 + \Delta V_{\alpha-\delta'}) \quad (9c)$$

When the transformed elements are then inserted back into the hole in the matrix, because of the constraint, these elements will readjust their sizes, and the inner and outer radius will finally be a and b. The displacements at the boundaries, as shown in Fig. 4, can be represented as,

$$u_1 = a - r_b = a - r_1(1 + \Delta V_{\alpha-\beta'})^{1/3} \quad (10a)$$

$$u_2 = a - r_{d1} = a - r_1(1 + \Delta V_{\alpha-\delta'})^{1/3} \quad (10b)$$

$$u_3 = b - r_{d2} = b - r_2(1 + \Delta V_{\alpha-\delta'})^{1/3} \quad (10c)$$

$$u_4 = b - r_2 \quad (10d)$$

where u_1 is the displacement in the inner sphere at $r = a$, u_2 and u_3 are the displacements in the hollow sphere at $r = a$ and $r = b$, respectively, and u_4 is the displacement in the infinite media at $r = b$. Using Equation 8, displacements at the boundaries can also be written as

$$u_1 = \frac{a}{E_C} P_1(\nu_C - 1) \quad (11a)$$

$$u_2 = \frac{a}{E_S}\left(\frac{3P_2b^3}{2(a^3 - b^3)} - \frac{P_1(2a^3 + b^3)}{2(a^3 - b^3)} + \nu_S P_1\right) \quad (11b)$$

$$u_3 = \frac{b}{E_S}\left(\frac{P_2(2b^3 + a^3)}{2(a^3 - b^3)} - \frac{3P_1a^3}{2(a^3 - b^3)} + \nu_S P_2\right) \quad (11c)$$

$$u_4 = \frac{b}{E_M} P_2\left(\frac{1}{2} + \nu_M\right) \quad (11d)$$

Combining Equations 10 and 11, for a given a and b, which are experimentally measurable constrained radii, four equations with four unknowns are obtained. These simultaneous equations can be solved by elimination and substitution to determine the unknowns P_1, P_2, r_1 and r_2. Using the calculated values of P_1 and P_2, the displacements in the composite precipitate shell and the surrounding matrix can be evaluated by use of Equation 8.

Two hypothetical cases were tested to check the relevance of the above developed approach. For this, the elastic properties of the phases and the total precipitate radius were kept constant. The elastic constant for all phases was taken as 70 GPa and the total precipitate radius as 50 nm. The core radius was changed sequentially from 10 nm to 40 nm by 10 nm increments. In the first case, the fractional volume changes due to transformation from matrix to core, $\Delta V_{\alpha-\beta'}$, and from matrix to shell, $\Delta V_{\alpha-\delta'}$, phases were taken as 0.02 and 0.01, respectively, assuming that both core and shell expand due to transformation. In the second case, however, the shell was assumed to shrink due to transformation by 1%, while the core expands by 2% as in the previous case. The radial strain distribution curves are shown in Fig. 5. It can be seen that, as expected, in all cases the strain distribution in the core region is uniform. In addition, in the first case, where both precipitate phases are expanded due to transformation, all the regions are in compression. However, in the second case, where the shell shrinks due to transformation, the expansion of the core is compensated by the shell when the core/total radius ratio is small, and the matrix remains in tension because the total precipitate is shrinking. However, when the core/total radius ratio reaches such a value that the volume expansion of the core region could no longer be compensated by the shrinkage of the shell, the total precipitate expands to set the matrix in compression.

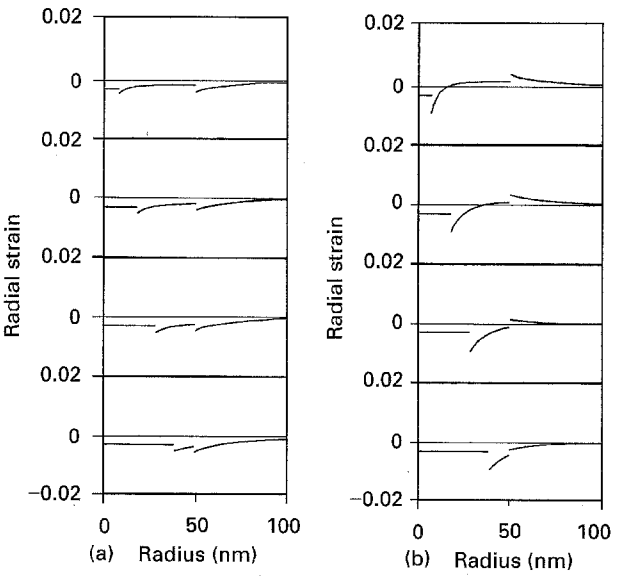

Figure 5 Calculated radial strain distribution in the composite precipitate geometry, assuming that the elastic constants of the phases are the same. The fractional volume changes due to transformation are (a) $\Delta V_{\alpha-\beta'} = 0.02$, $\Delta V_{\alpha-\delta'} = 0.01$ and (b) $\Delta V_{\alpha-\beta'} = 0.02$, $\Delta V_{\alpha-\delta'} = -0.01$. The total radius is 50 nm and the inner radius from top to bottom is 10, 20, 30 and 40 nm unit length.

4. Results and discussion

TEM observations on composite precipitates were made on a commercial Al–2.52Li–1.22Cu–0.68 Mg–0.15Zr alloy using a Jeol JEM 100CX electron microscope operated at 100 kV. Examples of superlattice dark field, $\boldsymbol{g} = (1\,0\,0)$, $s = 0$, images of composite precipitates are given in Fig. 6 to be compared and contrasted with the image simulation results presented below.

In calculation of the coherency displacement distribution in composite precipitates, the mismatch between the core (Al_3Zr) and matrix (aluminium), and shell (Al_3Li) and matrix phases were taken to be 1% [14] and −0.08% [15], respectively. The elastic constants of the aluminium matrix and Al_3Li shell were taken as 66 and 96 GPa [16], respectively, and for the Al_3Zr core it was assumed to be 120 GPa. In superlattice dark-field image simulations, five beams mentioned in the previous section were employed with $s_{(1\,0\,0)} = 0$ and the results are presented as grey scale

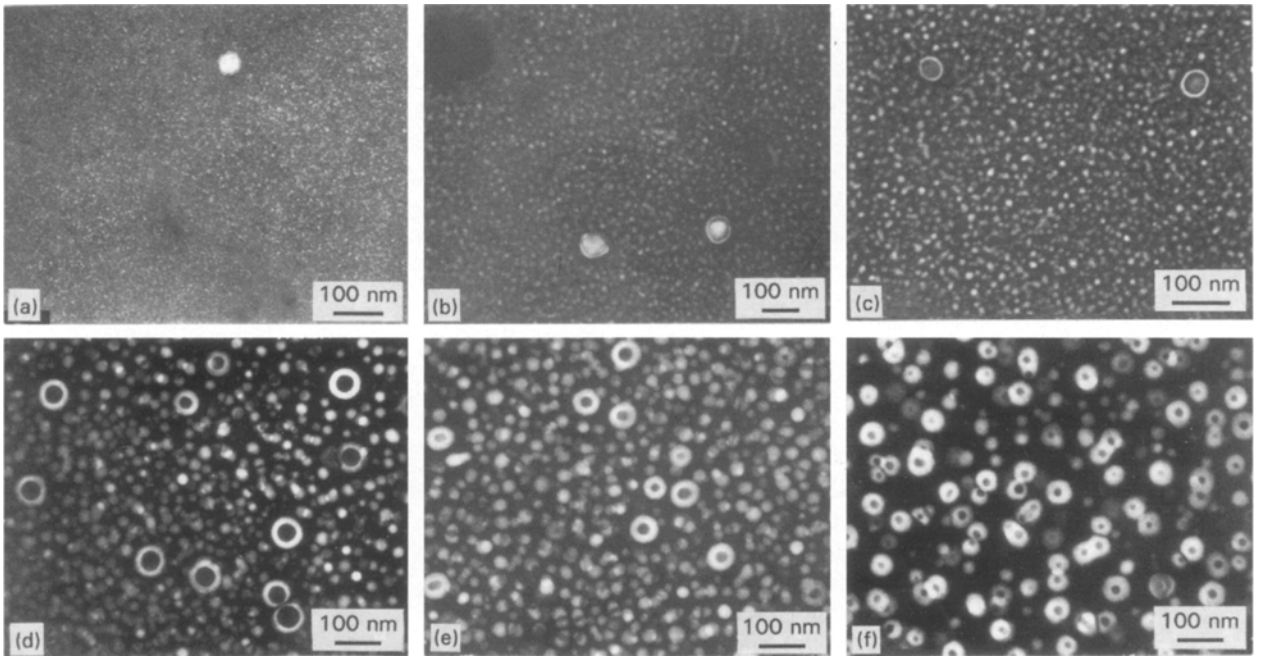

Figure 6 Superlattice dark-field TEM images of composite precipitates, $\boldsymbol{g} = (1\,0\,0)$, $s = 0$. Samples were (a) naturally, (b) 200 °C, 1 h, (c) 200 °C, 2 h, (d) 200 °C, 6 h, (e) 200 °C, 9 h and (f) 230 °C, 3 h aged.

pictures. Extinction and absorption distances used in the calculations are given in Table I.

The results of image simulations of composite precipitates are given in Fig. 7a and b without and with considering the effect of strain field, respectively. Fig. 7a shows the images that would be expected if the composite precipitates were not subject to the anomaly of an unknown origin. These completely bright images are definitely inconsistent with the experimental observations. Fig. 7b, which takes the strain

TABLE I Extinction and absorption distances (nm) of beams used in calculations for aluminium, Al_3Li and Al_3Zr phases for 100 kV electrons

	Al, $\xi_0' = 711.4$ nm		Al_3Li, $\xi_0' = 1080$ nm		Al_3Zr, $\xi_0' = 720$ nm	
hkl	ξ_g (nm)	ξ_g' (nm)	ξ_g (nm)	ξ_g' (nm)	ξ_g (nm)	ξ_g' (nm)
100	–	–	2155	26937	1589	19860
200	666	11258	804	10055	502	6281
300	–	–	6285	78560	2806	35075

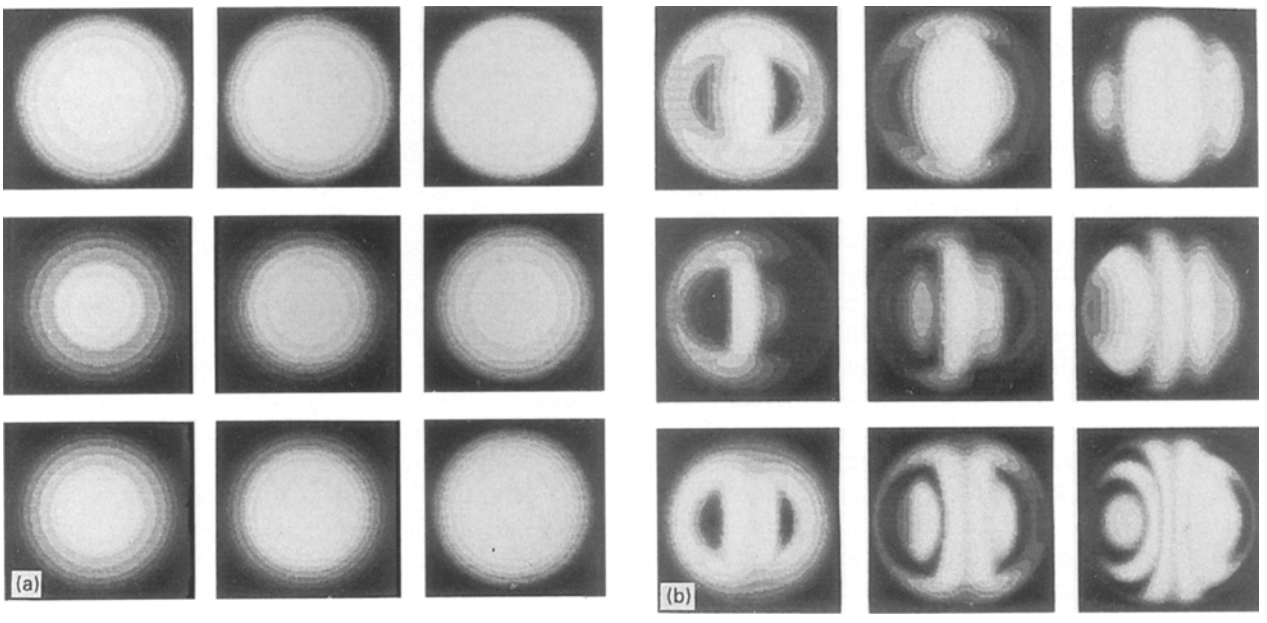

Figure 7 Simulated superlattice dark-field images of a composite precipitate, $\boldsymbol{g} = (1\,0\,0)$, $s = 0$, $t = 200$ nm, $r_{total} = 15$ nm. From left to right r_{core}/r_{total} ratio is 0.5, 0.7 and 0.9, and from top to bottom, the precipitate is located at 50, 100 and 150 nm from the top of the foil. Strain effects are not included in (a) and are included in (b).

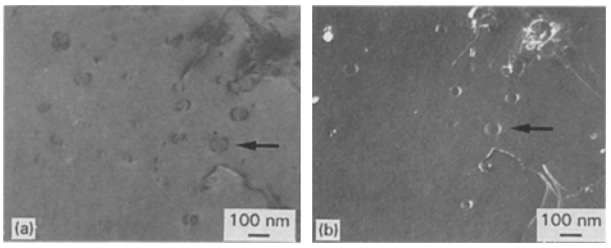

Figure 8 TEM image of coherent Al_3Zr precipitates in the aluminium matrix enveloped by a very thin shell of Al_3Li. (a) Bright-field image, $\boldsymbol{g} = (200)$, $s = 0$ and (b) weak-beam image, $s = -0.025\ nm^{-1}$.

effect into account, on the other hand, shows that the composite precipitate images should be extensively modified due to the presence of coherency strains at all core/total size ratios and at all depths of foil. But the modifications are not in the sense and/or extent to justify the experimental images. Composite precipitate images such as those given in Fig. 7b were never observed experimentally under any ageing conditions, Fig. 6, implying that coherency strain effects alone could not be responsible for the image characteristics of the composite precipitates.

The conclusion that the characteristic composite precipitate image could not have arisen from the strain effects, does not mean that there is no strain distribution around these precipitates or that the strain does not modify the images at all. It has been frequently observed that thin-shelled composite precipitates exhibit coherency strain contrast in bright-field or weak-beam dark-field TEM images, Fig. 8. Depending on the size of the precipitates and their position in the foil, images appear as two half lobes with a line of no contrast or as black and white lobes. The image width of the contrast of the precipitates in Fig. 8 seems to be considerably smaller than that expected from the 1% Al_3Zr/Al lattice mismatch obtained by lattice parameter calculations in a binary Al–0.18%Zr alloy [14] and employed in the present image calculations. The observed discrepancy in the mismatch value may be the result of an operative stress-relieving mechanism, such as interfacial misfit dislocation generation [1] or looping of matrix dislocations around the precipitates [17], but such dislocations were not observed experimentally in the present study. Then, there remains the possibility that the mismatch between the Al_3Zr precipitate and the aluminium matrix in the present alloy must have a smaller value. This has been tested by matching the simulated bright-field and weak-beam dark-field images for various mismatch values ranging from 0.1%–1%, Fig. 9, to the experimental precipitate images arrowed in Fig. 8. These results indicate that the mismatch between Al_3Zr precipitate and the aluminium matrix in the present Al–Li–Zr alloy should be about 0.3%. For an Al–1.1%Zr alloy, Izumi and Oelschlagel [18] have reported a mismatch value of 0.45% based on precipitate image analysis as described by Ashby and Brown [19] and assuming that matrix and precipitate elastic constants are equal.

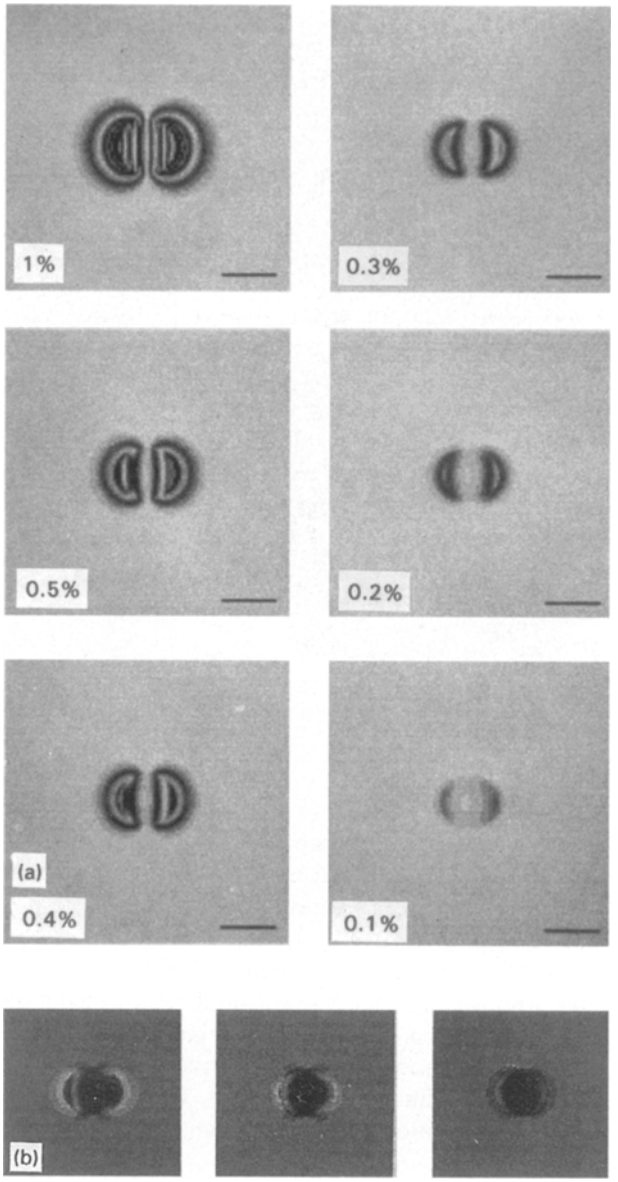

Figure 9 Simulated bright-field and weak-beam dark-field images of the composite precipitate arrowed in Fig. 8, using systematically reduced mismatch values between Al_3Zr and aluminium. $\boldsymbol{g} = (200)$, $t = 200$ nm, $r_{total} = 25.5$ nm, $r_{core} = 25$ nm and the precipitate is located at 100 nm from the top of the foil. (a) Bright-field simulations, $s = 0$. Mismatch values used in the calculations are indicated on the micrographs. The scale bar represents the actual total precipitate size. (b) Weak-beam dark-filed simulations, $s = -0.025\ nm^{-1}$. From left to right, the mismatch value is 0.4%, 0.3% and 0.2%, respectively.

Simulations done by reducing the elastic constant of Al_3Zr to 66 GPa, which is equal to the elastic constant of the aluminium matrix, has shown that the effect of the elastic constant is very weak and the experimental image in that case gives best fit to the simulated one with 0.35% mismatch.

To account for the possible error in mismatch value, additional superlattice dark-field composite precipitate images were simulated using systematically varied mismatch values, Fig. 10. It can be seen that, whatever the misfit value is, the calculated images are still not in conformance with the experimentally observed dark core–bright shell images of the composite precipitates.

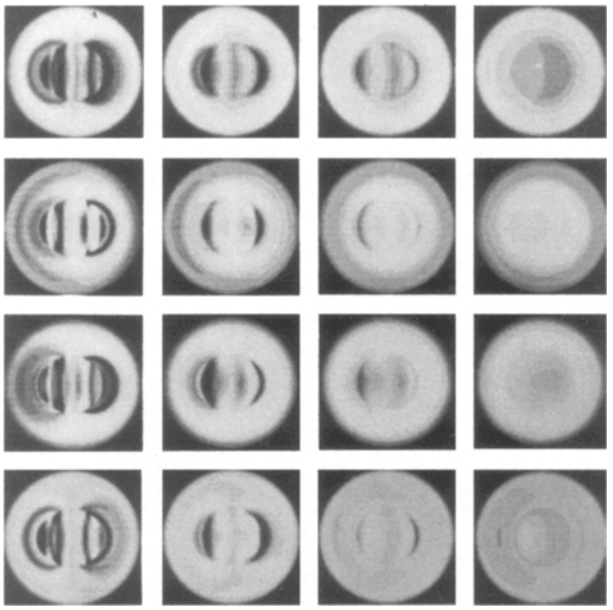

Figure 10 Simulated superlattice dark-field images of a composite precipitate, $g = (1\,0\,0)$, $s = 0$, $t = 250$ nm, $r_{total} = 405$ nm, $r_{core} = 18$ nm. From left to right, the mismatch value is 1%, 0.5%, 0.3% and 0.1%, and from top to bottom, the precipitate is located at 50, 100, 150 and 200 nm from the top of the foil.

5. Conclusion

Many beam dynamical image calculations have shown that the anomalous TEM image characteristics of composite precipitates in Al–Li–Zr alloys cannot be explained by the coherency strain field around these precipitates. The mismatch between the Al_3Zr precipitate and aluminium matrix in Al–Li–Zr alloys is found to be about 0.3%, which is considerably lower than the commonly accepted value of 1%.

References

1. P. L. MAKIN and B. RALPH, *J. Mater. Sci.* **19** (1984) 3835.
2. M. H. TOSTEN, J. M. GALBRAITH and P. R. HOWELL, *J. Mater. Sci. Lett.* **6** (1987) 51.
3. F. W. GAYLE and J. B. VANDERSANDE, *Scripta Metall.* **18** (1984) 473.
4. *Idem, Acta Metall.* **37** (1989) 1046.
5. P. L. MAKIN, D. J. LLOYD and W. M. STOBBS, *Philos. Mag.* **A51** (1985) L41.
6. P. J. GREGSON and H. M. FLOWER, *J. Mater. Sci. Lett.* **3** (1984) 829.
7. T. SATO, Y. KATO, A. KAMIO and T. TAKAHASHI, *Scripta Metall.* **23** (1989) 447.
8. W. STIMSON, M. H. TOSTEN, P. R. HOWELL and D. B. WILLIAMS, in "Proceedings of the 3rd International Conference on Aluminium–Lithium Alloys", Oxford, 1985, edited by C. Baker, P. J. Gregson, S. J. Harris and C. J. Peel (The Institute of Metals, London, 1986) p. 386.
9. P. B. HIRSCH, A. HOWIE, R. B. NICHOLSON, D. W. PASHLEY and M. J. WHELAN, "Electron Microscopy of Thin Crystals" (Butterworths, 1967) p. 276.
10. A. HOWIE and M. J. WHELAN, *Proc. R. Soc. Lond.* **A263** (1961) 217.
11. M. J. GORINGE, in "Electron Microscopy in Material Science", edited by U. VALDRE (Academic Press, New York, 1971) p. 463.
12. M. K. AYDINOL, PhD thesis, Middle East Technical University, Ankara, Turkey (1994).
13. S. TIMOSHENKO, "Theory of Elasticity" (McGraw-Hill, New York, 1934) p. 323.
14. E. NES, *Acta Metall.* **20** (1972) 499.
15. D. B. WILLIAMS and J. W. EDINGTON, *Metal Sci.* **9** (1972) 529.
16. B. NOBLE, S. J. HARRIS and K. DINSDALE, *J. Mater. Sci.* **17** (1982) 461.
17. L. M. BROWN and G. R. WOOLHOUSE, *Philos. Mag.* **21** (1970) 329.
18. O. IZUMI and D. OELSCHLAGEL, *Z. Metallkde* **60** (1969) 845.
19. M. F. ASHBY and L. M. BROWN, *Philos. Mag.* **8** (1963) 1083.

Received 22 December 1994
and accepted 13 February 1996